Improved low temperature sinter bonding using silver nanocube superlattices

Maxime Bronchy, Lucien Roach, Laurent Mendizabal, Céline Feautrier, Etienne Durand, Jean-Marc Heintz, Etienne Duguet, Mona Tréguer-Delapierre

▶ **To cite this version:**

Maxime Bronchy, Lucien Roach, Laurent Mendizabal, Céline Feautrier, Etienne Durand, et al.. Improved low temperature sinter bonding using silver nanocube superlattices. Journal of Physical Chemistry C, 2022, 126 (3), pp.1644-1650. 10.1021/acs.jpcc.1c09125 . hal-03558577

HAL Id: hal-03558577
https://hal.science/hal-03558577v1

Submitted on 4 Feb 2022

HAL is a multi-disciplinary open access archive for the deposit and dissemination of scientific research documents, whether they are published or not. The documents may come from teaching and research institutions in France or abroad, or from public or private research centers.

L'archive ouverte pluridisciplinaire **HAL**, est destinée au dépôt et à la diffusion de documents scientifiques de niveau recherche, publiés ou non, émanant des établissements d'enseignement et de recherche français ou étrangers, des laboratoires publics ou privés.

Improved Low Temperature Sinter Bonding using Silver Nanocube Superlattices

*Maxime Bronchy,[1,2] Lucien Roach,[1] Laurent Mendizabal,[2] Céline Feautrier,[3] Etienne Durand,[1] Jean-Marc Heintz,[1] Etienne Duguet,[1] Mona Tréguer-Delapierre[1]**

1. Univ. Bordeaux, CNRS, Bordeaux INP, ICMCB, UMR 5026, 33600 Pessac, France
2. CEA LETI, Univ. Grenoble Alpes, 38054 Grenoble, France
3. ASTEK Technology, 77T rue Marcel Dassault, 92100 Boulogne-Billancourt, France

KEYWORDS: silver, nanocubes, supercrystal, sintering, die-attach bonding device

ABSTRACT

We examined the potential of silver nanocubes to achieve sintered conductive junctions for applications in microelectronics and die-attach bonding devices. For such applications, it remains a challenge to achieve dense and robust joints, sintered at low temperature (< 200°C). The minimum sintering temperature is strongly dependent on the particle, interparticle distance and surface energy. In this respect, nanocubes offer two advantages over nanospheres: a higher proportion of surface atoms and the ability to assemble into denser 3D colloidal packings. Here, we used a colloidal approach to create joints using 3D close-packed arrays of silver nanocubes of different edge lengths (from 20 to 60 nm). Starting from monodisperse nanocubes, we assembled

them into close-packed supercrystals by drop-casting and investigated their thermal stability and electrical properties on silicon nitride substrates. Spectroscopic measurements allowed correlation of the plasmonic signature with the length and the degree of corner curvature of the cubes. Using electron microscopy and electrical measurements, we studied the impact of the nanocube size on the sintering temperature and electric properties of the self-organized arrays. The small gaps between the building-units yielded uniform sintered patterns possessing high electrical conductivity. More broadly, our approach shows how Ag particles featuring a high density of low-coordination surface atoms, separated by small gaps, increase the efficiency of sintered Ag technology for microelectronics.

INTRODUCTION

Silver has an array of properties which can be tuned or enhanced through the control of nanoscale size and morphology for a variety of applications.[1-3] The field of nanowelding exploits the different thermal behavior of nano-sized particles compared to bulk materials,[4-5] which enables the formation of conductive metallic junctions at low temperature.[6-12] This is of high interest for the fabrication of electronic devices on flexible substrates and for power semiconductor devices.[11,12] It remains a challenge to produce junctions with excellent mechanical, thermal and electrical properties after sintering at temperature below 200°C. The sintering process of nanoparticles is highly dependent on their surfaces characteristics.[4,5,13,14] Many groups have examined the effects of size and surface coating sinter bonding using spherical nanoparticles.[14-19] It is now well-established that small silver nanoparticles undergo rearrangement at temperatures well below their bulk melting point (T_m = 962 °C). Oxygen exposure activates the surface rearrangement processes,

typically at 300°C.[15,17] The organic coating adsorbed onto the surface of metallic nanoparticles is difficult to remove at temperatures below 200°C. Consequently, many pores form during the decomposition of these organics, lowering the final density and electrical conductivity of the sintered joint. The influence of particle shape on sintering processes remains relatively unexplored.[20-24] An anisotropic diffusion of surface atoms between neighboring nanowires or nanochesnuts alongside substantial heat-induced morphological changes have been observed during sintering. These changes accelerate the sintering process in some directions, however they leave many voids between the sintered zones.[16,19, 23,24]

Here, we report about the potential of silver nanocubes arrays to achieve thick silver joints at low temperature and at ambient pressure. We focus on the creation of conductive junction with cubic nanocrystals because they offer a higher fraction of reactive surface atoms and favor the formation of close-packed 3D superlattices. Nanocubes of fcc metals with {100} facets have numerous unstable low-coordinated corner and edge atoms.[25] These surface atoms have increased mobility allowing them to move across surface facets and migrate to neighboring particles. Moreover, when compared to spherical building blocks, organized arrays of cubes have higher packing fractions and large contact interfaces, which favors the exchange of atoms during the sintering process.[26-28] Our strategy can be broken down into three steps as shown in Scheme 1. We first synthesized monodisperse silver cubes in high shape yield. Then, we self-assembled them into 3D ordered arrays and lastly investigated their thermal and electrical behaviors upon annealing in air.

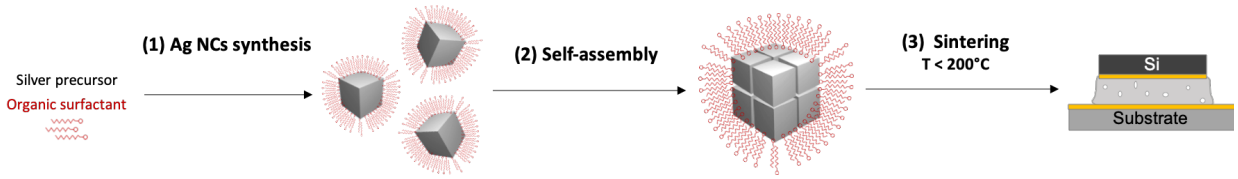

Scheme 1. Scheme Showing the Low-Temperature (LT) Fabrication of Silver Joint Investigated in This Study Following Three Steps: (1) Colloidal Synthesis of Nanocubes (2) Self-Assembly into Close-Packed Supercrystals by Drop Casting (3) Thermal Annealing Treatment to Induce the Sintering into Dense Joints.

MATERIALS AND METHODS

Materials

Silver nitrate ($AgNO_3$, 99.99%, Sigma-Aldrich), silver trifluoroacetate (CF_3COOAg, 99.99%, Sigma-Aldrich), cetyltrimethylammonium chloride (CTAC, 98%, Sigma-Aldrich), sodium borohydride ($NaBH_4$, 98%, Sigma-Aldrich), *L*-ascorbic acid (L-AA, 98%, Sigma-Aldrich), 1*H*,1*H*,2*H*,2*H*-perfluoro-1-decanethiol (97%, Sigma-Aldrich), deionized water (DI water, 18.2 MΩ·cm) and absolute ethanol (Atlantic Labo) were used as received without further purification.

Synthesis of size-tunable silver nanocubes

We used a two-step protocol to synthesize silver nanocubes in aqueous medium (scheme of the Figure 1a), inspired by the work of Lin *et al.*[29] In the first stage, Ag seeds were prepared in a 25 mL round-bottom flask immersed in an oil bath set to 30°C. 10 mL of CTAC aqueous solution (0.5 mM) was introduced in the flask and stirred using a Teflon-coated magnetic bar. After 10 min, 25 µL of a freshly prepared $AgNO_3$ aqueous solution (0.1 M) was introduced in the flask and left to homogenize for 5 min. Next, 450 µL of an ice-cold $NaBH_4$ aqueous solution (40 mM) was quickly injected into the reaction medium under rapid stirring. The reaction medium was aged under stirring for 1 h at 30°C to decompose excess of $NaBH_4$ by water. The size of the as-obtained

silver seeds was found to be 5 ± 1 nm by transmission electron microscopy (TEM). The second stage consisted of re-growing these Ag seeds after transfer of part of the reactive medium into a 100 mL flask containing a given volume of DI water under stirring at 60°C (Table 1). Then 500 µL of a CF_3COOAg aqueous solution (0.1 M) were added and the reactive medium was aged for 20 min, before quickly adding 5 mL of an L-AA aqueous solution (0.1 M).

Table 1: Experimental conditions of the seeded-growth stage of the Ag nanocubes.

Cube edge length (nm)	**20**	**24**	**28**	**35**	**45**	**60**
Seed solution vol. (mL)	7.50	5.00	2.50	1.50	0.50	0.25
DI water vol. (mL)	37.00	39.50	42.00	43.00	44.00	44.25

After 90 min, the Ag particles were isolated by centrifugation and resuspended in 2 mL DI water threefold (15 000 *g*, 20 min). Finally, the Ag nanocubes were redispersed in 2 mL of DI water. For the scale-up synthesis, the flask was replaced by a 1 L round bottomed flask, and the volume of all solutions was increased by a factor of ten.

Preparation of supercubes by drop casting

The Ag nanocube dispersions (15 μL droplet concentration) were deposited onto silicon nitride substrates (Si_3N_4, Au metallization, active metal brazed (AMB) substrate), previously treated by plasma cleaning. Then, were immersed in a 50 mL of 1 mM 1*H*,1*H*,2*H*,2*H*-perfluoro-1-decanethiol ethanolic solution for 24 h under slow stirring (100 rpm) and then dried at room temperature. The deposited dispersion was evaporated at 22°C in a closed environment (glass bell) until total solvent evaporation (~3 h) enabling nanoparticle self-assembly into close-packed structures. The as-prepared deposition was then stored under argon. We estimated the interparticle distance within the assemblies essentially by microscopic imaging at high magnification.

Sintering of the paste

The heating was carried out, in air, at different temperatures, for 2 h using a hotplate. The nanocube arrays were characterized before and after sintering by means of scanning electron microscopy (SEM) and electrical resistance measurements.

Characterization techniques

Electron Microscopy. Scanning transmission electron microscopy (STEM) studies were performed using a JEOL cold-FEG JEM-ARM200F operating at 200 kV equipped with a probe Cs corrector reaching a spatial resolution of 0.078 nm. Energy Dispersive X-Ray (EDX) spectra were recorded on a JEOL CENTURIO SDD detector. For the TEM experiments, samples were prepared by depositing one drop (~3 µL) of the colloidal dispersion onto a conventional carbon-coated copper grid. Grids were dried in air at room temperature and stored in a closed box to prevent dust accumulation. They were analyzed using a JEOL JEM 1400+ operating at 120 kV with a LaB_6 filament. SEM experiments were performed on a SEM-FEG HR - JEOL 6700F. The characterization was performed on different points of the samples to assess the homogeneity in surface and within the volume as well as identify the intertwined parameters: macro-porosities, density and the characteristic lengths of the metallic joint after sintering. By image analysis, the surface area of the cross-sections could be measured and its ratio with the total surface area observed, allowing the porosity of the sintered joint to be assessed. For cross-sectional images, a diamond tip cutter was used to break the assemblies (and the substrates) to expose the transverse surfaces.

Optical characterization. UV-vis spectroscopy spectra were recorded on a Shimadzu UV-3600 UV-vis-NIR (cuvette path length: 1 cm). The Fourier transform infrared (FT-IR) spectra were collected using a Shimadzu MIRacle 10 IR spectrophotometer, depositing a droplet of the as-

prepared nanocubes suspension on the detection cell. The optical responses of the nanocubes were simulated using COMSOL's radio frequency module. Calculations were performed in the frequency domain in the scattered field formulation using the PARDISO direct solver. Refractive index values for Ag were taken from Johnson & Christy.[30] Particles were simulated embedded in a medium of water (n = 1.333) surrounded by a perfectly matched layer. σ_{abs} was calculated through a volume integral of the resistive heat losses inside the silver nanocube, Q_{rh}. σ_{scat} was calculated through a surface integral of the Poynting vector, at the particle surface.

Thermal and electrical measurements. Thermogravimetric analysis (TGA) was used to investigate the thermal decomposition of the organics at 5 °C·min^{-1} under air (TG Setsys 'Evo' Apparatus from Setaram). The sheet resistance of the metal layer deposited, typically on a silicon substrate of width of 1 cm and length of 1 cm, was measured using four-point probe measurements (RTS-9, 4 Probes Tech.). The volume resistivity of the metal pattern was calculated from the sheet resistance together with the metal layer thickness determined by SEM images. Five sets of assemblies were deposited and isolated from each other for measurements.

RESULTS

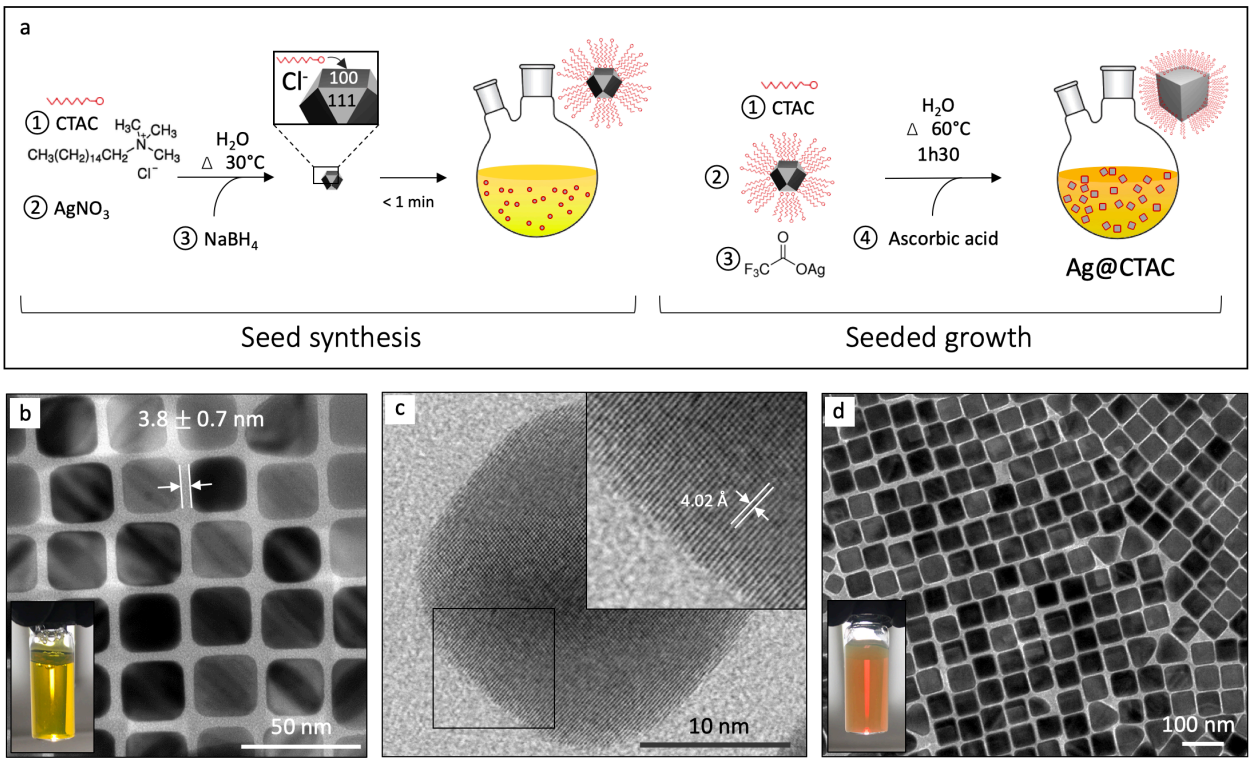

Figure 1. **(a)** Scheme of the colloidal synthesis adopted **(b)** TEM image of Ag nanocubes of edge length, $L = 20 \pm 3$ nm that can be synthesized at high yield by our approach **(c)** High-resolution image of an individual Ag nanocube (inset: a magnified section of the selected area). **(d)** TEM image of larger cubes with average $L = 60 \pm 7$ nm. The insets of the Figure 1(b) and (d) are photographs of the corresponding reaction solution.

We first synthesized size-monodisperse silver cubes in aqueous medium by optimizing a previously reported method (Figure 1).[29] This method takes dual advantage of the CTAC molecules as shape-inducing agent in step 1 and self-assembly promoter of the supercrystals in step 2 of the Scheme 1. TEM analysis showed that the synthesis was successful and revealed the close proximity of the particles to each other once deposited on a TEM grid (Figure 1b). The seeded growth provides size-monodisperse Ag nanocubes in high yield relative to other shapes (bipyramids and a few triangular plates). The overall morphology yield of the synthesis is ~85%. Because of their high uniformity, the as-obtained cubes self-assemble into regions of square closed-packed monolayer. The CTAC adsorption on the particles surface was confirmed by FT-

IR analysis (Figure S1). As the amount of CTAC per cube is too low, no specific ligand patterning modes on surface could be revealed by HRTEM and elemental mapping (Figure 1c and S2).

By controlling the molar ratio between seeds and silver salt, the edge length, *L*, of the cubes was successfully tuned from 20 to 60 nm and the shape and size dispersion was weak (Figure 1 and S3). Synthesizing Ag nanocubes with $L < 20$ nm, remains challenging due to the limited self-diffusion distance of silver atoms. Typically cubes with $L < 20$ nm exhibit radii of curvature, *r*, on their corners which are a higher proportion of their edge length (Figure S4). The typical optical extinction spectrum of a Ag cube sample features a marked localized surface plasmon resonance (LSPR) band centered at ~410 nm and weaker resonances between 350 nm and 390 nm (Figure 2). The major band is due to a dipolar mode while the weak shoulder bands correspond to higher-order plasmonic modes localized at the corners and edges of the cubes.[31] The distinct well-separated extinction peaks seen in the experimental spectra confirm the structural features of Ag cubes with sharp edges. The weak bands seen around ~350 nm consistently maintained a peak extinction around this wavelength as L was tuned between 20 and 60 nm. In contrast, the major peak shifted between 407 nm to 460 nm as the size increases. The dependence of the major LSPR peak, λ_{max}, on L is linear between 400 and 460 nm. This is in good quantitative agreement with finite element modelling (FEM) simulations of the expected optical properties of cubes of the same average dimensions synthesized here (Figure 2b and c), as well as results reported elsewhere.[32-33] The exact position of λ_{max} is highly sensitive to the radius of curvature, *r*, of the cubes at the edges and corners, red-shifting with decreasing values of *r*. Hence, the average value of *r* obtained from TEM images were used to in the simulated geometries of each sample. It can be seen from the simulated absorption and scattering cross sections (Figure S5) that the optical response of smaller

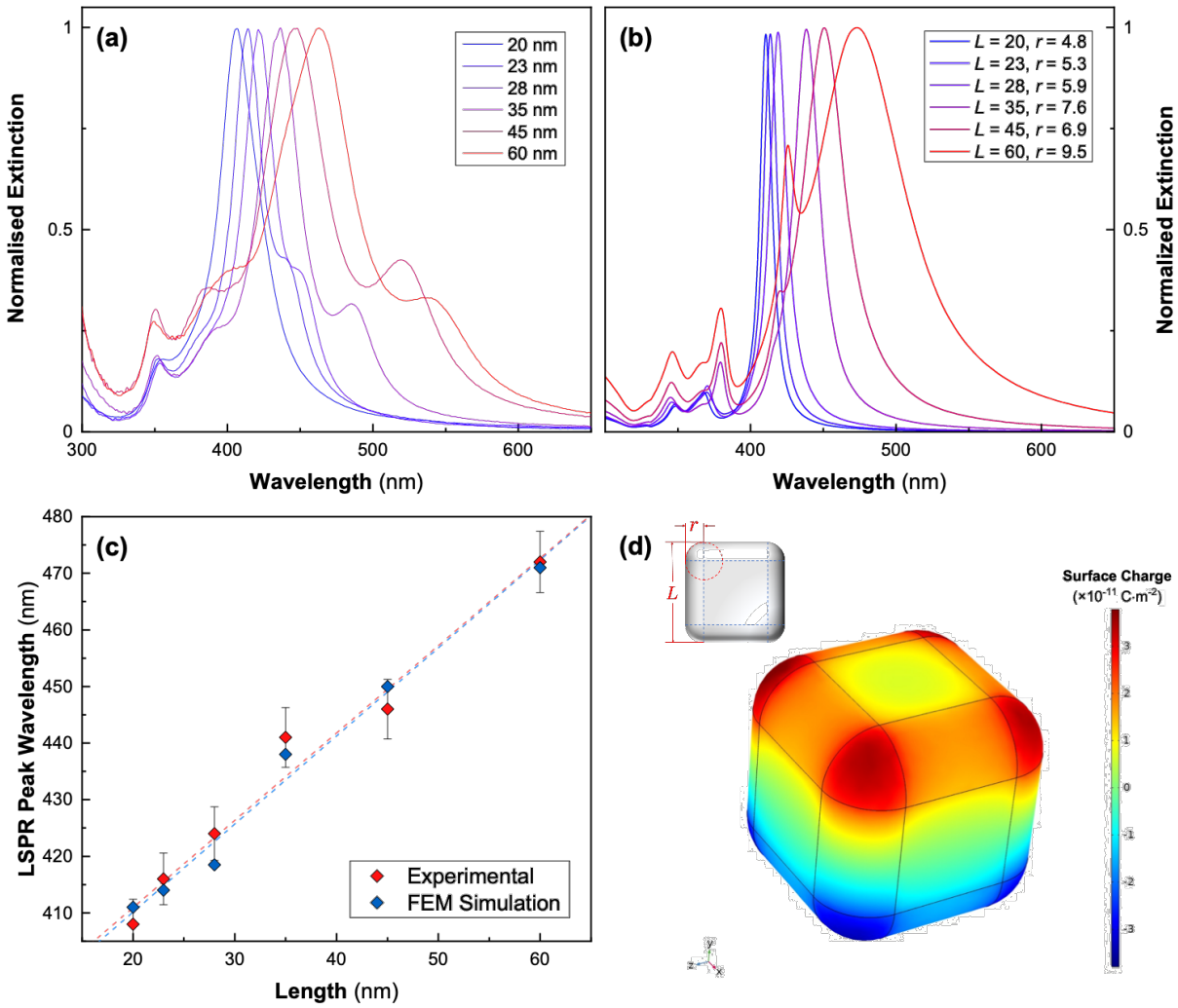

Figure 2. (a) Normalized UV-vis extinction spectra of the synthesized Ag nanocube samples with tunable sizes. **(b)** FEM simulated spectra of silver nanocubes of the same average edge length, L, and radius of corner curvature, r (in nm) as the experimentally measured samples in (a). **(c)** LSPR peak wavelength for both experimental and finite element modeling (FEM) simulated extinction spectra as function of L with corresponding linear fits. **(d)** Surface charge distribution for a Ag nanocube of $L = 20$ nm and $r = 4.8$ nm with excitation in the y direction ($|E_0| = 1$ V·m^{-1}). **Inset:** schematic showing the geometry used in the simulations, with r and L labelled.

cubes is dominated by the absorbance whereas the response of larger cubes is predominantly scattering. In the simulated spectra, the optical response of nanocubes smaller than 35 nm are

dominated by the electric dipolar resonance (Figure 2d & S6). For 35 nm nanocube, the electric quadrupolar mode appears as a shoulder at ~440 nm, and is a distinct peak from the dipolar mode in the extinction spectrum for larger sizes 55 nm. These features are obscured in the experimental

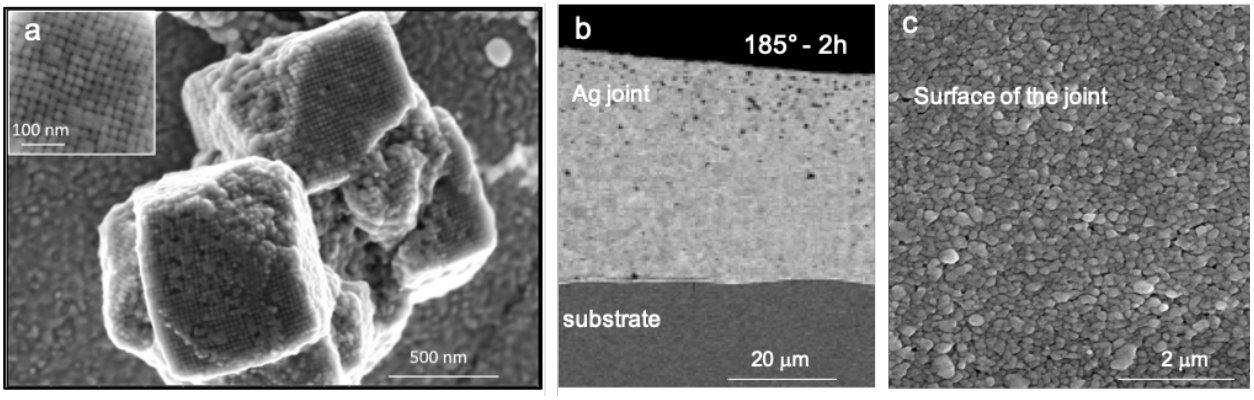

Figure 3. SEM images of densely packed Ag nanocube superstructures (L = 20 nm) **(a)** before and **(b**,**c)** after heating. **inset**: top-view SEM image of silver nanocube arrays before heating **(b)** cross-sectional view of the silver cube joint after uniform heating on a hotplate **(c)** top-view of the same sample.

spectra probably because of polydispersity in the sample, leading to the quadrupolar mode appearing as a shoulder in the spectra of larger cubes. The extra peak in between 500 and 525 nm, observed for some of colloidal suspensions, is caused by an in-plane dipole plasmon resonance, which has been seen in the bipyramid byproducts.[31] The long-term stability of the Ag nanocube solution stored under ambient condition was confirmed by spectral analysis. The extinction spectra acquired from samples stored for one year are unchanged compared to those taken immediately after the synthesis (not shown). Moreover, we show that the synthesis can be upscaled up to 0.3 grams by increasing the volume of all solutions by a factor of 10. In this case, the synthesis follows the same observed color changes as seen at smaller volumes suggesting that the growth mechanism does not change as the reaction volume increases.

The Ag nanocubes assemble spontaneously into 3D tetragonally packed patterns, as mediated by the CTAC surfactant, upon a slow and controlled evaporation of the solvent on a hydrophilic

substrate. Figure 3a shows a SEM micrograph of the as-obtained supercubes composed of Ag nanocrystals of $L \sim 20$ nm prior to annealing. Independent of the size of the building units, the nanocrystals assemble face-to-face to form simple cubic superlattices with lateral dimensions up to 3 μm. The interparticle spacing within the cubic lattice is ~3-4 nm as determined from measurements of TEM and SEM images close to the cell boundary (inset of the Figure 1b and Figure 3a). This distance is consistent with the thickness of two partially interdigited CTAC bilayers.[36, 37] In larger assemblies (10-50 μm), the symmetry of the simple cubic lattice can be more broken, space-filling packing are observed.

After an annealing treatment at 185°C, for 2 h, in air on an AMB substrate, a homogeneous sintered layer is obtained due to ligand removal (Figure 3b and c). As shown in the cross-sectional and surface views, all the nanocubes, separated by nanogaps, have coalesced giving rise to a typical sintered microstructure. The sintering is uniform throughout the whole volume of the sample. Moreover, the sintered joint exhibit proper adhesion and cohesion on the substrate. Some pores can be observed close to the surface of the joint. This may be related to the decomposition pathway of the organic surfactant and its gaseous elimination towards the surface. The surface view shows that the closed-packed nanocrystals have lost their cubic morphology and collapsed uniformly into grains of about 150-200 nm. The density of the metal joint is estimated to 0.94 ± 0.02 by imaging analysis of the sectional cross-section (Figure S7). It is slightly lower on the first surface layers due to the some voids between the sintered zones. It can be noted that, at 150°C, even below the temperature of decomposition of the organic ligand, the sintering is already very well-advanced (Figure S8). The TGA analysis reveals that the overall amount of CTAC decomposed is close to 8% (Figure S9). Some residual CTAC may be trapped into the voids of the porous structure, but it is difficult to estimate its proportion. The resistivity of the joint was measured to be (3.9 ± 0.1)

μΩ·cm, which is very close to that of bulk silver (1.59 μΩ·cm).[37] This performance is attributable to a very good sintering process of the metal nanosurfaces, separated by nanoscale gaps, at 185°C, leading to an uniform sintered microstructures with a high density of fused particles. Similar results were observed on arrays of larger nanocrystals with L up to 60 nm (Figure S10). No significant changes in thermal and electric behaviors as function of particle size could be detected at the microscopic scale (Table S1). It would be interesting to undertake further work to address the *in situ* characterization of the heating-induced coalescence processes to get better understanding on the atomic surface diffusion intra- and inter-particles at atomic level. No drastic electric change occur in the size range 20-60 nm, owing to the small difference of the fraction of the surface atoms of the cubes. But the diffusion processes could vary with crystallite size and inter-particle distance. There are a few experimental reports and detailed models of the morphological evolution of nanocubes in response to variations in temperature.[14,23,38,39] Typically the surface atoms of nanoparticles become effectively liquid-like below the melting point of the interior volume of the nanoparticle. Surface atoms becoming increasingly mobile allowing them to drive the coalescence and sintering of neighboring particles. Previous work, at single particle level, has convincingly shown that this atomic reorganization is highly dependent on the crystal geometry (nanocube imperfection(s)) and surface coating.[5,39] During which new facets are formed and/or there are changes to the relative areas of the existing facets. Not surprisingly, the most mobile atoms are situated at corners and edges.[14] They are also the most active sites for the initiation of coalescence and sintering. Some scanning tunneling microscopy (STM) studies tracked, in real time and with atomic resolution, the basic progression in the morphological states during the sintering process from initially separated corner-to-corner cubes to the final sintering state.[14,19] During the initial stages of coalescence, atoms from the outer corners of neighboring particles move towards the

centers of the flat facets until a neck is formed between the opposing facets of neighboring particles. As the coalescence process progresses, the cubes evolve into a nanorice with a rounded profile. There is a qualitative size dependence on the atomic diffusion kinetics.[14] The coalescence process between two particles increases in speed with decreasing nanocrystal size. Therefore, it seems probable that the coalescence will be accelerated for supercrystals composed of cubes with $L < 20$ nm. But, it remains challenging to have a high degree of control over the morphology when the lengths become smaller than 20 nm.

CONCLUSION

This work illustrates the potential of organized arrays of Ag nanocrystals for low temperature sintered electronics device applications. The close packed arrays of nanocubes favors small gaps between the surfaces of metallic particles, enabling their uniform sintering in three dimensions upon heating. The sintering yields high density joints with few voids at 185°C yielding junctions that possess a high conductivity. This opens up exciting new, simple, and large-area processing schemes that are facilitated by the rapid coalescence and sintering of nanocrystal arrays at lower temperature. Further work may investigate the thermal behavior of arrays of cubes with a higher fraction of surface atoms located on the corners and the edges, i.e with L < 20 nm or even lower. Furthermore, this strategy could be extended to binary superlattices. In which, the introduction of a second population of smaller nanocubes could facilitate neck formation between the corners of larger ones where voids currently form. Modern colloidal techniques allow for the synthesis of a a wide range of well-defined polyhedral nanocrystalline shapes and control of their interparticle distances during evaporative self-assembly. Combining these two techniques offers the prospect of forming binary lattices through the self-assembly of polyhedral shapes, other than cubes, to

generate junctions containing different geometries of voids and gaps. This will allow new levels of control over mass transport at the nanoscale that needs to be further explored.

ASSOCIATED CONTENT

Supporting Information. The following file is available free of charge. Supplementary Data: Additional figures related to FT-IR and TGA profiles of the CTAC-capped Ag nanocubes, size dispersity of the colloidal samples, SEM images of the assemblies after sintering (PDF), and FEM simulations of optical properties and surface charge.

AUTHOR INFORMATION

Corresponding Author

*mona.treguer@icmcb.cnrs.fr

Author Contributions

The manuscript was written through the contributions of all authors.

ACKNOWLEDGMENTS

TEM and STEM-EDX experiments were performed at the Plateforme de Caractérisation des Matériaux of the University of Bordeaux (UMS 3626 CNRS) and Centre de Micro-Caractérisation R.Castaing of the University of Toulouse (UMS 3623 CNRS). We thank Teresa Hungria-Hernandez for some HRTEM analysis of the samples. M. Bronchy is particularly indebted to CEA LETI for the funding of his thesis grant.

ABBREVIATIONS

CTAC, cetyltrimetylammonium chloride; L-AA, L-ascorbic acid; TEM, transmission electron microscopy; SEM, scanning electron microscopy; STEM, scanning transmission electron microscopy; EDX, Energy Dispersive X-Ray; FT-IR, Fourier transformed infrared; TGA, Thermogravimetric analysis; FEM, finite element modelling.

REFERENCES

[1] Wiley, B.; Sun, Y.; Xia, Y. Synthesis Of Silver Nanostructures With Controlled Shapes And Properties. *Acc. Chem. Res.* **2007**, *40*, 1067-1076.

[2] Lee, S.; Jun, B. Silver Nanoparticles: Synthesis And Application For Nanomedicine. *Int. J. Mol. Sci.* **2019**, *20*, 865.

[3] Cherqui, C.; Bourgeois, M.; Wang, D.; Schatz, G. Plasmonic Surface Lattice Resonances: Theory And Computation. *Acc. Chem. Res.* **2019**, *52*, 2548-2558.

[4] Luo, W.; Hu, W.; Xiao, S. Size effect on the Thermodynamic Properties of Silver Nanoparticles. *J. Phys. Chem. C* **2008**, *112*, 2359-2369.

[5] He, L.; Zhang, L.; Tan, X.; Tang, L.; Xu, T.; Zhou, Y.; Ren, Z.; Wang, Y.; Teng, C.; Sun, L. et al. Surface Energy and Surface Stability of Ag Nanocrystals at Elevated Temperatures and Their Dominance in Sublimation-Induced Shape Evolution. *Small* **2017**, *13* (27), 1700743.

[6] Wang, T.; Chen, X.; Lu, G.; Lei, G. Low-Temperature Sintering with Nano-Silver Paste in Die-Attached Interconnection. *J. Electron. Mater.* **2007**, *36*, 1333-1340.

[7] Wakuda, D.; Chang-Jae Kim, C.; Keun-Soo Kim, K.; Suganuma, K. Room Temperature Sintering Mechanism of Ag Nanoparticle Paste. **2008** *2nd Electronics System Integration Technology Conference* 2008, 909-914.

[8] Magdassi, S.; Grouchko, M.; Berezin, O.; Kamyshny, A. Triggering the Sintering of Silver Nanoparticles at Room Temperature. *ACS Nano* **2010**, *4*, 1943-1948.

[9] Knoerr, M.; Kraft, S.; Schletz, A. Reliability Assessment of Sintered Nano-Silver Die Attachment for Power Semiconductors. **2010** 12th *Electronics Packaging Technology Conference* 2010, 56.

[10] Suganuma, K.; Sakamoto, S.; Kagami, N.; Wakuda, D.; Kim, K.; Nogi, M. Low-Temperature Low-Pressure Die Attach with Hybrid Silver Particle Paste. *Microelectron. Reliab.* **2012**, *52*, 375-380.

[11] Venkata Krishna Rao, R.; Venkata Abhinav, K.; Karthik, P. S.; Surya Prakash, S. Conductive Silver Inks and Their Applications in Printed and Flexible Electronics. *RSC Adv.* **2015**, *5*, 77760-77790.

[12] Wu, W. Inorganic Nanomaterials for Printed Electronics: a Review. *Nanoscale* **2017**, *9*, 7342-7372.

[13] Ding, J.; Liu, J.; Tian, Q.; Wu, Z.; Yao, W.; Dai, Z.; Liu, L.; Wu, W. Preparing of Highly Conductive Patterns on Flexible Substrates By Screen Printing of Silver Nanoparticles with Different Size Distribution. *Nanoscale Res. Lett.* **2016**, *11*, 412.

[14] Lai, K.; Han, Y.; Spurgeon, P.; Huang, W.; Thiel, P.; Liu, D.; Evans, J. Reshaping, Intermixing, and Coarsening for Metallic Nanocrystals: Nonequilibrium Statistical Mechanical and Coarse-Grained Modeling. *Chem. Rev.* **2019**, *119*, 6670-6768.

[15] Thompson, C. Grain Growth In Thin Films. *Annu. Rev. Mater. Sci.* **1990**, *20*, 245-268.

[16] Ferrando, R.; Tréglia, G. Anisotropy of diffusion along steps on the (111) faces of gold and silver. *Phys. Rev. B* **1994**, *50*, 12104.

[17] Thiel, P.A.; Evans, J.W. Nucleation, Growth, and Relaxation of Thin Films: Metal (100) Homoepitaxial Systems. *J. Phys. Chem. B* **2000**, *104*, 1663-1676.

[18] Asoro, M.; Kovar, D.; Ferreira, P. *In situ* Transmission Electron Microscopy Observations of Sublimation in Silver Nanoparticles. *ACS Nano* **2013**, *7*, 7844-7852.

[19] Han, Y.; Stoldt, C.; Thiel, P.; Evans, J. Ab Initio Thermodynamics and Kinetics for Coalescence of Two-Dimensional Nanoislands and Nanopits on Metal (100) Surfaces. *The J. Phys. Chem. C* **2016**, *120* (38), 21617.

[20] Yeom, J.; Nagao, S.; Chen, C.; Sugahara, T.; Zhang, H.; Choe, C.; Li, C.; Suganuma, K. Ag Particles for Sinter Bonding: Flakes or Spheres? *Appl. Phys. Lett.* **2019**, *114*, 253103.

[21] Peng P.; Hu, A.; Zhao, B; Gerlich, A. Zhou, Y.N. Reinforcement of Ag nanoparticle Paste with Nanowires for low Temperature Pressureless Bonding. *J. Mater. Sci.* **2012**, *47*, 6801-6811.

[22] Zhao S.Y; Li X., Mei, Y.H.; Lu G.Q. Effect of Silver Flakes in Silver Paste on the Joining Process and Properties of Sandwich Power Modules (IGBTs Chip/Silver Paste/Bare Cu). *J. Electron. Mater.* **2016**, *45*, 5789-5799.

[23] Lee, J.; Lee, J.; Tanaka, T.; Mori, H. *In Situ* HRTEM Observation of Crystalline-to-Gas Transition in Nanometer-Sized Ag Particles. *Phys. Rev. Lett.* **2006**, *96*, 075504.

[24] Li, J.; Wang, Z.; Li, Y.; Deepak, F. *In Situ* Atomic-Scale Observation of Kinetic Pathways of Sublimation in Silver Nanoparticles. *Adv. Sci.* **2019**, *6* (8), 1802131.

[25] Van Hardeveld, R.; Hartog, F. The Statistics of Surface Atoms and Surface Sites on Metal Crystals. *Surf. Sc.* **1969**, *15*, 189-230.

[26] Gantapara, A.; de Graaf, J.; van Roij, R.; Dijkstra, M. Phase Diagram and Structural Diversity of a Family of Truncated Cubes: Degenerate Close-Packed Structures and Vacancy-Rich States. *Phys. Rev. Lett.* **2013**, *111*, 015501.

[27] Henzie, J.; Grünwald, M.; Widmer-Cooper, A.; Geissler, P.; Yang, P. Self-Assembly of Uniform Polyhedral Silver Nanocrystals into Densest Packings and Exotic Superlattices. *Nat. Mater.* **2011**, *11*, 131-137.

[28] Courty, A.; Henry, A.I. ; Goubet, N. ; Pileni, M.-P. Nat. Mater. Large triangular single crystals formed by mild annealing of self-organized silver nanocrystals, *Nat. Mater.* **2007**, *6*, 900-907.

[29] Lin, Z.; Tsao, Y.; Yang, M.; Huang, M. Seed-Mediated Growth of Silver Nanocubes in Aqueous Solution with Tunable Size and Their Conversion to Au Nanocages with Efficient Photothermal Property. *Chem. Eur. J.* **2016**, *22*, 2326-2332.

[30] Johnson, P.B. and Christy, R.W. Optical Constants of the Noble Metals. *Phys. Rev. B* **1972**, 6, 4370.

[31] Cherqui, C.; Li, G.; Busche, J.A. ; Quillin, S.C. ; Camden, J.P. ; Masiello, D.J. 'Multipolar Nanocube Plasmon Mode-Mixing in Finite Substrates' *J.Phys.Chem.Lett.* **2018**, 9, 504-512.

[32] Sekhon, J. S.; Malik, H. K.; Verma, S. S. 'DDA Simulations of Noble Metal and Alloy Nanocubes for Tunable Optical Properties in Biological Imaging and Sensing' *RSC Adv.* **2013**, 3, 15427.

[33] Yaraki, M.T.; Rezaei, S.D.; Tan, Y.N. Simulation Guided Design of Silver Nanostructures for Plasmon-Enhanced Fluorescence, Singlet Oxygen Generation and SERS Applications. *Phys. Chem. Chem. Phys.*, **2020**, *22*, 5673-5687.

[34] Wiley, B. J.; Xiong, Y.; Li, Z.; Yin, Y.; Xia, Y. Right Bipyramids of Silver: a New Shape Derived from Single Twinned Seed. *Nano Lett*. **2006**, *6*, 765-768.

[35] Boles, M.A.; Engel, M.; Talapin, D.V. Self-Assembly of Colloidal Nanocrystals: from Intricate Structures to Functional Materials. *Chem. Rev.* **2016**, *116*, 11220-11228.

[36] Gomez-Grana, S.; Hubert, F.; Testard, F.; Guerrero-Martinez, A.; Grillo, I.; Liz-Marzan, L.; Spalla, O. Surfactant (Bi)Layers on Gold Nanorods, *Langmuir* **2012**, 28, 1453-1459.

[37] Matula, R.A., Electrical Resistivity of Copper, Gold, Palladium, and Silver, *J.Phys.Chem.Ref.Data* **1979**, 8, 1147.

[38] Lee, J.-G.; Lee, J.; Tanaka, J.; Mori, H. In Situ HRTEM Observation of Crystalline-To-Gas Transition in Nanometer-Sized Ag Particles. *Phys. Rev. Lett.* **2006**, *96*, 75504.

[39] Ding, Y.; Fan, F.; Tian, Z.; Wang, Z. Sublimation-Induced Shape Evolution of Silver Cubes. *Small* **2009**, *5*, 2812-2816.

[40] Lai, K.C., Evans, J.W., Reshaping and Sintering of 3D fcc Metal Nanosclusters: Stochastic Atomic Modeling with a Realistic Surface Diffusion Kinetics. *Phys. Rev. Mater.* **2019**, *3*, 026001.

[41] Liu, D.J.; Evans, J.W.; Sintering of Two-Dimensional Nanoclusters in Metal (100) Homoepitaxial Systems: Deviations froom Predictions of Mullins Continuum Theory. *Phys. Rev. B: Condens. Matter* **2002**, *66*, 165407.

[42] Stoldt, C.R; Cadhile, A.M., Jenks, C.J.; Wen, J.M.; Evans, J.W. Thiel, P.A. Evolution of Far-from-Equilibrium Nanostructures Formed by Cluster-Step and Cluster-Cluster Coalescence in Metal Films, *Phys. Rev. Lett.* **1998**, *81*, 2950.

TOC Graphic